Applied Thermal Engineering 236 (2024) 121572

Contents lists available at ScienceDirect

Applied Thermal Engineering

journal homepage: www.elsevier.com/locate/ate

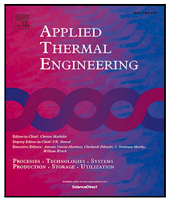

Research Paper

New structure-performance relationships for surface-based lattice heat sinks

D. Padrão [a], D. Hancock [b], J. Paterson [b], F. Schoofs [b], C. Tuck [a], I. Maskery [a,*]

[a] Centre for Additive Manufacturing, University of Nottingham, Nottingham NG8 1BB, UK
[b] United Kingdom Atomic Energy Authority, Culham Science Centre, OX14 3DB, Abingdon, UK

ARTICLE INFO

Keywords:
Cellular structure
Lattice
Fluid flow
Conjugate heat transfer
Computational fluid dynamics (CFD)

ABSTRACT

Heat sinks have manifold applications, from micro-electronics to nuclear fusion reactors. Their performance expectations will continue to increase in line with the power consumption and miniaturisation of technology. Additive manufacturing enables the creation of novel, compact heat sinks with greater surface-to-volume ratios and geometrical complexities than standard pin/fin arrays and pipes. Despite this, there has been little research into the use of high surface area lattice structures as heat sinks. Here, the hydraulic and thermal performance of five surface-based lattice structures were examined numerically. Computational fluid dynamics was used to create useful predictive models for pressure drop and volumetric heat transfer coefficients over a range of flow rates and volume fractions, which can henceforth be used by heat transfer engineers. The thermal performance of surface-based lattices was found to be heavily dependent on internal geometry, with structures capable of distributing thermal energy across the entire fluid volume having greater volumetric heat transfer coefficients than those with only localised areas of high heat transfer and low levels of fluid mixing.

1. Introduction

Additive manufacturing (AM) describes a range of processes which join materials to make solid parts from 3D model data, usually layer upon layer. Metal AM offers enhanced design freedom compared to conventional processes, enabling the production of near-net shape components with complex internal geometries and high customisability, such that parts can be tailored for specific applications and users [1]. This technology was initially developed for rapid prototyping, but is now used in several sectors to produce final products, such as in aerospace [2] where the GE LEAP fuel nozzle has been a notable commercial success [3].

The incorporation of 3D cellular structures is a key element of AM design. Ordered lattices (as opposed to the typically random foams that can be made with gas injection [4], for example) have received significant attention in the literature [5], and are now available in several commercial CAD packages aimed at AM. They reduce component weight, have high surface-to-volume ratios and high solid–fluid contact areas [1,4], making metal lattices in particular ideal candidates for heat sinks [6–8]. Compared to lattices composed of interconnected struts or 'trusses', triply periodic minimal surface (TPMS) lattices have enclosed channels for fluid flow, greater surface areas, and are generally stiffer and stronger at equivalent weight [9]. Therefore, TPMS lattices offer unique advantages for fluid flow and heat transfer applications.

Heat sinks are common devices, with applications ranging from micro-electronics [10] to nuclear fusion [11], which typically employ channels or extended surfaces, such as pin/fin arrays, to dissipate heat. The dominant heat transfer mechanisms for these structures under laminar flow are convection in the fluid flow direction and conduction in the direction normal to that. For turbulent flow, heat transfer is driven by convection in the fluid [12]. TPMS lattice structures can be considered as an alternative to conventional geometries as they promote convective cooling due to their large surface areas. Conversely, these features also lead to greater pressure drops, and potentially lower heat sink efficiencies [13].

The need to dissipate large quantities of heat from small volumes will continue to increase in line with the increased power demands and miniaturisation of electronic devices. It is therefore necessary for heat sinks to be maximally efficient, in terms of their size and material usage. Despite this, there has been little research on the use of complex surface-based cellular structures within AM heat sinks, with much of the published work dedicated to foams [14–17], strut-based lattices [18–23], topology-optimised structures [24] or conventional pin/fin arrays and channels [21,25–29]. Recently, heat transfer in TPMS structures has garnered some attention, with applications including heat sinks/exchangers [30–40], injection mold cooling [41] and latent heat thermal energy storage systems [42–44]. These studies characterise the thermal performance of TPMS lattice structures with varying wall thicknesses and in a range of flow conditions. These need to be developed further, so that engineers can use well-understood structure-performance relationships when incorporating TPMS lattice

* Corresponding author.
E-mail address: ian.maskery@nottingham.ac.uk (I. Maskery).

https://doi.org/10.1016/j.applthermaleng.2023.121572
Received 2 May 2023; Received in revised form 30 August 2023; Accepted 7 September 2023
Available online 12 September 2023

Nomenclature

ΔT_{LMTD}	Logarithmic mean temperature difference (K)
$\dot{m}$	Mass flow rate (kg s^{-1})
A_v	Specific surface area (m^2/m^3)
$A_{w,s}$	Wetted surface area (m^2)
c_p	Specific heat capacity (J kg^{-1} K^{-1})
D_h	Hydraulic diameter (m)
F	Parameter correlating Nu_{vol} to Re
h_l	Local wall heat transfer coefficient (W m^{-2} K^{-1})
$h_{m,vol}$	Volumetric heat transfer coefficient (W m^{-3} K^{-1})
h_m	Global mean heat transfer coefficient (W m^{-2} K^{-1})
K	Darcian permeability (m^2)
k	Thermal conductivity (W m^{-1} K^{-1})
K_1	Forchheimer permeability (m^2)
K_2	Inertial permeability (m)
L	Channel length (m)
n	Parameter correlating Nu_{vol} to Re
Nu_{vol}	Volumetric Nusselt number
P	Fluid pressure (Pa)
R_a	Arithmetic average roughness (μm)
Re	Reynolds number
$T_{f,in}$	Fluid inlet temperature (K)
$T_{f,out}$	Fluid outlet temperature (K)
T_h	Heating temperature (K)
T_s	Average channel surface temperature (K)
u_m	Mean channel fluid velocity (m s^{-1})
u_s	Superficial fluid velocity (m s^{-1})
V_T	Total volume of design space (m^3)
V_w	Wetted volume (m^3)
γ	Volume fraction
μ	Dynamic viscosity (kg m^{-1} s^{-1})
ν	Kinematic viscosity (m^2 s^{-1})
ρ	Density (kg m^{-3})

geometries in heat sinks. These relationships can also be used in conjunction with other such rules, like the Gibson–Ashby scaling laws for stiffness or thermal conductivity [5], to design multifunctional components which, for example, provide maximal stiffness and thermal transport within a given weight restriction.

Pulvirenti et al. [30] conducted a numerical study into the gyroid matrix lattice at low Reynolds numbers. The authors found that the lattice structure was characterised by local volumetric heat transfer coefficients similar to those of other periodic structures, such as the Kelvin geometry [16,17]. Santos et al. [45] examined the permeability of a range of TPMS lattice structures and found that the fluid flow was described by the Darcy–Forchheimer law, which is helpful in identifying designs for efficient lattice-based heat sinks. Concerning the permeability of foams, Della Torre et al. [46] found an exponential dependence of the permeability on porosity, supporting the notion that porosity can be a useful design parameter for specifying flow in analogous AM lattices. Maloney et al. [18] found the thermal conductance of a micro-strut-based lattice heat exchanger to be determined by various geometrical features such as node-to-node spacing and lattice member diameter. Feng et al. [38] and Mahmoud et al. [39] explored how different geometrical parameters, such as cell aspect ratio, can impact the thermal performance of surface-based lattice structures. These studies provide an overall framework to develop structure-performance relationships for flow and heat transfer in AM cellular structures.

This paper examines the hydraulic and thermal transfer performance of TPMS-based lattice geometries over a range of fluid flow velocities and volume fractions. We establish design guides for fluid flow and heat transfer in these lattices in terms of their principal geometrical properties. Section 2 describes the methodology for our work, with Sections 2.1–2.3 providing details about the design of lattices and numerical modelling. Sections 3 and 4 contain the main results and discussion of this study. Concluding remarks are given in Section 5.

Table 1
Specific surface areas for the examined TPMS-based lattice structures with dimensions of 10 × 50 × 10 mm containing 1 × 5 × 1 lattice cells.

Volume fraction	Specific surface area (m^2/m^3)				
	DM	GM	LM	PM	SPM
0.15	761	613		466	1,016
0.2	755	608	1,194	462	1,008
0.25	747	602	1,171	457	996
0.3	737	594	1,149	450	981
0.35	725	584	1,119	441	964
0.4	711	574	1,086	431	944

2. Methodology

2.1. Cellular structures

Five TPMS lattice structures were chosen for this study. These were the diamond matrix (DM), gyroid matrix (GM), lidinoid matrix (LM), primitive matrix (PM) and split-p matrix (SPM) lattices. The DM, GM and PM lattices were chosen as they have received the most attention in the literature, whereas the remaining structures were chosen for their tortuous channels and high surface areas. The examined structures are illustrated in Fig. 1.

Each examined structure had dimensions of 10 × 50 × 10 mm containing 1 × 5 × 1 lattice cells. These were chosen to provide sufficient surface to allow the fluid to develop fully and to examine the evolution of mixing arising from the periodicity of the structures. To develop general structure-performance models for arbitrary lattice geometries, the fluid dynamics within the lattice cells must first be understood. For this reason, the structures examined here comprise a single unit cell in the directions normal to fluid flow.

The TPMS lattice structures were generated using FLatt Pack, a research-focused lattice design program [47]. TPMS-based lattice structures can be subdivided into ‘network’ and ‘matrix’ forms, where the matrix forms were used in this study as they possess greater surface areas per unit volume [48]. A network phase lattice consists of two continuous regions, one solid and one void. A matrix phase lattice has three continuous regions, two of which are void with equivalent geometries, with the other being a solid separating wall. For heat exchange applications, network lattices can exchange heat between a solid and a fluid while matrix lattices can exchange heat between two fluids across a solid barrier. One of the key geometrical properties of TPMS lattice structures is volume fraction, γ, defined as the ratio between solid volume and design space volume. This can be controlled, for TPMS matrix lattices, by modifying the thickness of the walls. The volume fraction of the examined structures in this study ranged from $\gamma = 0.15 - 0.4$ which corresponded to the specific surface areas (i.e., ratio of wetted surface area to design space volume) given in Table 1. It can be seen here that the LM structure has the greatest specific surface areas while the PM structure has the lowest.

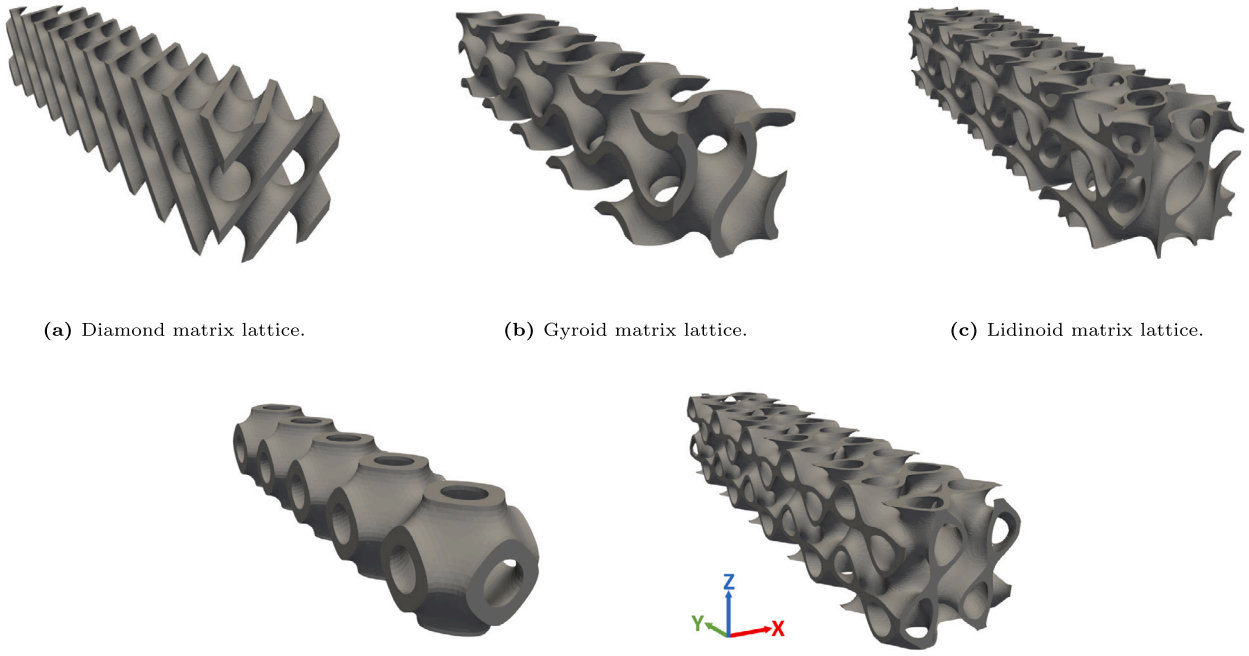

(a) Diamond matrix lattice. **(b)** Gyroid matrix lattice. **(c)** Lidinoid matrix lattice.

(d) Primitive matrix lattice. **(e)** Split-p matrix lattice.

Fig. 1. Examined structures (shown with a volume fraction of 0.25).

2.2. Computational method

Computational fluid dynamics (CFD) was used here to model fluid flow and conjugate heat transfer. Numerical results were obtained using OpenFOAM v1812 [49], an open-source CFD software written in C++. A conjugate heat transfer solver, *chtMultiRegionSimpleFoam*, was used to model incompressible, steady-state fluid and heat transfer between different bodies, where the solid region is modelled with the heat conduction equation and the fluid–solid solutions are coupled at the common boundaries by imposing continuity of temperature and heat flux.

Our CFD models included a fluid domain of dimensions 10 × 90 × 10 mm, which encapsulate the solid lattice test structure. Inlet and outlet pipes were used, 20 mm in length each. This was sufficient for the flow to develop and transition in to the structures and to prevent the propagation of any divergent results upstream from the outlet. The *snappyHexMesh* utility was used to import STL representations of the lattice structures into the computational domain to provide CFD meshes. Finally, a constant-temperature boundary condition at 323 K is applied to the base of the modelled solid and fluid domains within the lattice structures to simulate the effect of a heater. Heating was applied in one direction in order to be more closely analogous to real applications (e.g., liquid cooling of a CPU or GPU) and to examine the impact of a directional heat source. The fluid-solid boundary was modelled as a smooth interface. This was chosen instead of a rough interface, which may be more reflective of AM components generally, in order to obtain useful structure-performance relationships applicable across a range of manufacturing and materials scenarios. The effect of surface roughness on the fluid dynamics was also found to be negligible when considering arithmetic average roughnesses, R_a, of 10 μm, which is representative of metal upward-facing surfaces produced from a range of AM materials and processes [50–53]. This was determined by examining flow through a gyroid lattice with and without the inclusion of a rough surface. We observed no appreciable difference in the resulting fully developed flow or heat transport. The schematics of the computational domain of a circular channel model (used for numerical validation) are given in Fig. 2.

Water was modelled in both fluid domains with a density, ρ, of 1000 kg m^{-3}, a kinematic viscosity, ν, of 8.9 × 10^{-7} m^2 s^{-1} and assumed to be incompressible. The fluid travelled in the y-direction, with inlet flow rates of $u_s = 0.8 \times 10^{-3} - 6 \times 10^{-3}$ m s^{-1}, corresponding to $Re = 3.2 - 62.5$. This flow regime was examined to ensure that there would be significant differences between results at different flow rates and such that the performance of these structures can be meaningfully compared with other work in the literature, such as that of Pulvirenti et al. [30] and Santos et al. [45].

Flow in our CFD models was defined by the *noSlip* boundary condition (BC) at the walls and fluid boundaries, forcing the fluid velocity to zero, and the *pressureInletOutletVelocity* BC at the outlet, where a zero-gradient condition was applied for outflow. The inlet flow was defined by a *fixedValue* BC, which fixes the velocity to a specified value. The pressure at the outlet was defined by a *fixedValue* BC and the inlet was defined by a *fixedFluxPressure* BC, which sets the pressure gradient such that the flux is specified by the fluid velocity BC. The temperature of the fluid domain was defined by an *inletOutlet* BC of 293 K applied to the inlet fluid and a *zeroGradient* (adiabatic) BC at the outlet and outer walls. A *zeroGradient* BC was applied to the outlet because the profile of the outlet temperature was not known and to prevent error propagation upstream. The solid domain was modelled as Inconel-718 (which has seen extensive use in heat sinks in the aerospace industry [2]), with a density of 8190 kg m^{-3}, specific heat capacity of 435 J kg^{-1} K^{-1} and a thermal conductivity of 11.4 W m^{-1} K^{-1}. These boundary conditions are well-established for finite-volume modelling and have been used to accurately predict fluid flow and heat transfer [17,31,46].

A CFD mesh convergence study was performed to determine a suitable mesh element density for accurate fluid flow and conjugate heat transfer predictions. This was performed for a GM lattice structure (γ = 0.4) at a volumetric flow rate of 6 × 10^{-7} m^3 s^{-1}. The pressure drop and outlet fluid temperature were found to be well converged at around 1.8 million elements, as shown in Fig. 3, for an unstructured mesh featuring refined polyhedral elements at the fluid-solid boundaries and hexahedral elements elsewhere (see Fig. 4). The models used throughout this work therefore feature similar meshes.

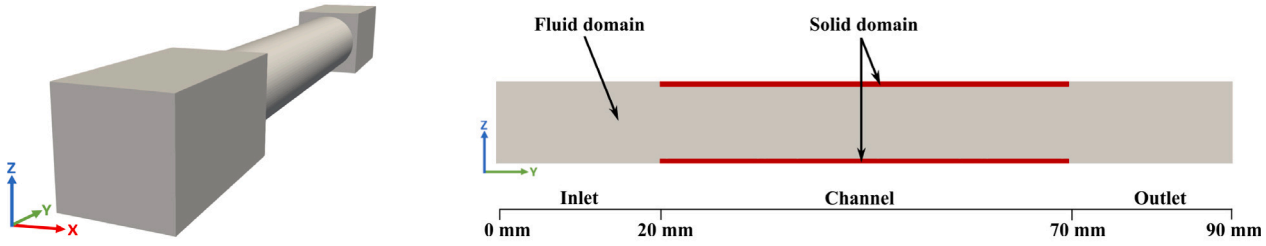

(a) Fluid domain.

(b) Cross-sectional view with the fluid domain (grey) and solid domain (red).

Fig. 2. Schematics for the computational domain of a simple circular channel.

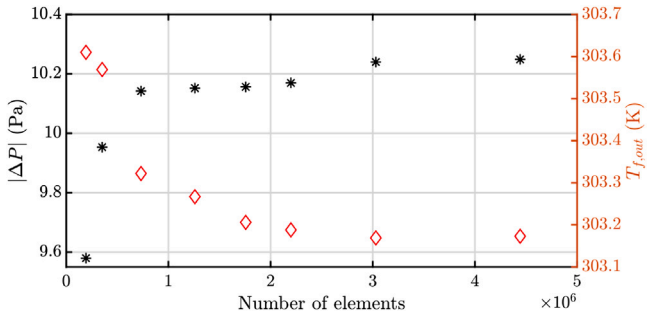

Fig. 3. Pressure drop (black star) and outlet fluid temperature (red diamond) mesh convergence analysis for a gyroid matrix lattice (superficial fluid velocity = 6×10^{-3} m s^{-1}, volume fraction = 0.4).

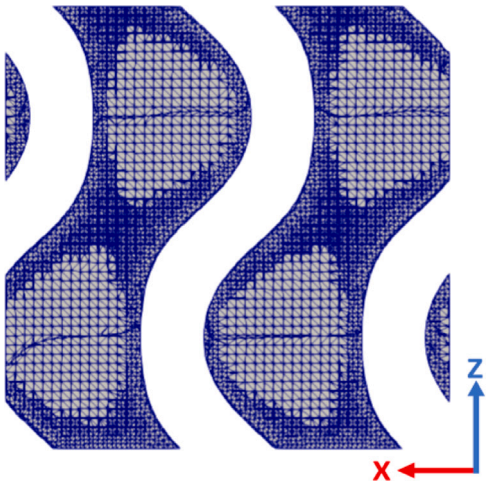

Fig. 4. Mesh elements in the fluid domain for a gyroid matrix lattice with a volume fraction of 0.4 at a position $y = 0.025$ m after the inlet.

A convergence study was also performed for a GM lattice structure (γ=0.4) to determine whether a turbulence model was necessary to model the fluid and heat transfer accurately. This was done because the tortuous channels of TPMS structures may promote turbulence and, as will be discussed in Section 2.3, the examined flow range is in the laminar-turbulent transition region for a porous structure [54]. The pressure drop from the RANS (Reynolds-averaged Navier–Stokes) $k-\epsilon$ turbulence model agreed with the results from a laminar solver and the fluid exit temperature from the RANS $k-\epsilon$ turbulence model was within 0.4% of that which was predicted by a laminar solver, as shown in Fig. 5. A turbulence model was therefore deemed unnecessary for this study.

Our CFD model was first validated against the numerical results presented by Pulvirenti et al. [30], where we obtained differences of 1.4% and 0.01% for the pressure drop and fluid exit temperature, respectively, for an equivalent GM structure. For completeness, we used our CFD model to predict fluid flow in a simple circular channel. This was validated against the Hagen–Poiseuille law, with our numerical model predicting pressure drops within 1% of the analytical solution.

2.3. Theoretical background and method

Pressure drop, ΔP, across the test structures was examined to determine the hydraulic performance of each lattice type. In addition, the fluid dynamics and variation of fluid pressure within the structures were examined to understand the impact of different lattice geometries at equivalent volume fractions.

Darcy's law describes pressure drop across a porous medium for slow, viscous flow [45]

$$\left|\frac{\Delta P}{\Delta L}\right| = \frac{\mu}{K} u_s \,, \tag{1}$$

where $\Delta P/\Delta L$ is the pressure drop per unit length, μ is the dynamic viscosity, K is the Darcian permeability constant and u_s is the superficial fluid velocity. At high flow rates, where the flow is no longer in the Darcy regime, a non-linear term is added to account for inertial effects. This is known as the Forchheimer term [55]. We have

$$\left|\frac{\Delta P}{\Delta L}\right| = \frac{\mu}{K_1} u_s + \frac{\rho}{K_2} {u_s}^2 \,, \tag{2}$$

where K_1 is the Forchheimer permeability constant and K_2 is the inertial permeability constant. The permeability constants are in general associated with the geometry of the porous medium, where K and K_1 represent the viscous drag and K_2 is linked to the blockage of the internal geometry [55]. It is important to note that K and K_1 are not the same. This is because transitioning from a Darcian to a Forchheimer flow regime implies changes to the viscous and inertial drags [55,56]. It is vital to know which regime applies to the flow in a particular structure, in order to use the appropriate model. This was achieved by rearranging Eq. (2) to obtain

$$\left|\frac{\Delta P}{\Delta L\, u_s}\right| = \frac{\mu}{K_1} + \frac{\rho}{K_2} u_s \,, \tag{3}$$

which was then used to fit pressure drop data [55]; any part which is linear with u_s is Forchheimer flow.

Reynolds numbers are also quoted in this work as they provide more general descriptions of fluid flow and can be compared to other studies, which may use different initial conditions and geometries. The Reynolds number for a porous structure is [15]

$$Re = \frac{u_s\, D_h}{\nu\,(1-\gamma)} \,, \tag{4}$$

where D_h is the hydraulic diameter. The transition region between laminar and turbulent flow for porous structures exists for $10 < Re < 2000$ [54].

D_h for porous structures was calculated using [15]

$$D_h = 4\frac{V_w}{A_{w,s}} \,, \tag{5}$$

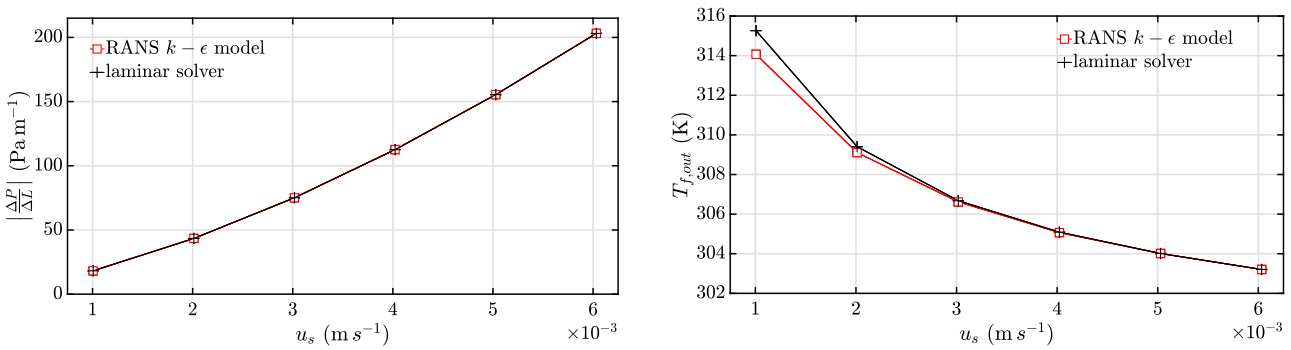

(a) Pressure drop. **(b)** Fluid exit temperature.

Fig. 5. Comparison between the RANS $k-\epsilon$ model and a laminar solver for a gyroid matrix with a volume fraction of 0.4.

where V_w is the wetted volume and $A_{w,s}$ is the wetted surface area, which was extracted from the CAD representations of the lattice structures. This approach was used to estimate the hydraulic diameter as it takes into account the complexity of different lattice types across the entire fluid domain. Different lattice types therefore experience different Reynolds numbers at equivalent inlet flow rates, which more accurately reflects the fluid flow compared to the assumption of equal *Re*.

Heat transfer performance was examined through mass flow rate weighted averages of heat transfer coefficients and Nusselt numbers. Two different heat transfer coefficients were used, the first being a local wall heat transfer coefficient, h_l. This was calculated directly in OpenFOAM using the Reynolds analogy model, which relates the wall shear stress to heat transfer [57,58]. Due to it being a local variable, it can be used to determine points of high and low heat transfer within the examined structures.

The global, mean heat transfer coefficient, h_m, was also examined. It is given by [20]

$$h_m = \frac{\dot{m} c_p \left(T_{f,out} - T_{f,in}\right)}{A_{w,s} \Delta T_{LMTD}}, \tag{6}$$

where $\dot{m}$ is the fluid mass flow rate, c_p is the fluid specific heat capacity, $T_{f,out}$ and $T_{f,in}$ are the fluid outlet and inlet temperatures and ΔT_{LMTD} is the logarithmic mean temperature difference. ΔT_{LMTD} was given by

$$\Delta T_{LMTD} = \frac{T_{f,out} - T_{f,in}}{\ln\left(\frac{T_h - T_{f,in}}{T_h - T_{f,out}}\right)}, \tag{7}$$

where T_h is the heating temperature. This definition of ΔT_{LMTD} has been used previously by Dixit et al. [20], but an alternative definition uses the average channel surface temperature, T_s, in place of T_h [25]. T_h was used here because $T_h - T_{f,in}$ gives the initial temperature difference in the structures [43], whereas using T_s gives the heat transfer over the entire fluid-solid interface, the size of which varies significantly between lattice designs. T_s is also not representative of the large distribution of surface temperatures present in TPMS lattice structures, as observed by Al-Ketan et al. [32].

In this study, the volumetric heat transfer coefficient, $h_{m,vol}$, was used instead of h_m as it is independent of the surface area (which differs for different lattice structures at equivalent volume fraction). This was obtained from [16]

$$h_{m,vol} = h_m A_v, \tag{8}$$

where A_v is the specific surface area.

The volumetric Nusselt number gives the ratio of convective to conductive heat transfer for a fluid and is an alternative way to express heat transfer performance. This was defined by [16]

$$Nu_{vol} = \frac{h_{m,vol} {D_h}^2}{k}, \tag{9}$$

where k is the thermal conductivity of the fluid. This is a dimensionless quantity and can be used alongside *Re* to compare structures under different flow conditions.

3. Results

3.1. Hydraulic performance

Pressure drop for a range of volume fractions and flow rates are presented in Fig. 6, where ΔP is calculated by finding the difference between inlet and outlet average pressure. Fig. 6 shows that ΔP increases non-linearly with both u_s and γ and that the LM lattice exhibits the greatest pressure drop across the examined ranges while the PM lattice exhibits the lowest pressure drop in most cases. At low volume fractions the GM lattice exhibits greater pressure drop than the PM structure. This behaviour switches as volume fraction increases, indicating that a particular lattice geometry may not be treated as inherently more efficient than others, with performance also being dependent on fluid flow conditions.

Examining the evolution of fluid pressure, taken as a cross-sectional average (Fig. 7), we see that pressure decreases linearly along the flow direction in the GM, DM and LM structures, despite the tortuous nature of the channels. This is not replicated in the PM or SPM structures, which instead exhibit step-like pressure drops.

This can be explained by examining the flow within the structures, as shown in Fig. 8. Regarding the PM structure, the majority of the fluid passes through a central volume or 'channel'. However, as the channel diameter decreases at the cell boundary, some fluid is recirculated in the characteristic chambers of the PM lattice, appearing as eddies. The PM geometry therefore acts as a series of bottlenecks, providing sharp pressure drops within the structure. This can also be observed in the SPM lattice, but to a lesser degree. Flow is not periodically impeded in the remaining structures because their internal geometry does not possess such large variations in channel diameter, minimising fluid recirculation. Whilst the SPM and LM lattices appear to have similar geometries and flow dynamics in Fig. 8, implying that they should share similar pressure characteristics within the structures, their three-dimensional geometry differs significantly. The dominant factor behind pressure drop for TPMS structures is therefore the channel diameter, where smaller channels lead to larger pressure drops, shown in Fig. 9, and where changes in the diameter lead to localised pressure drops.

Before calculating the permeability constants, the flow regime must be determined. We found $\Delta P / \left(\Delta L\, u_s\right)$ to increase linearly with u_s for

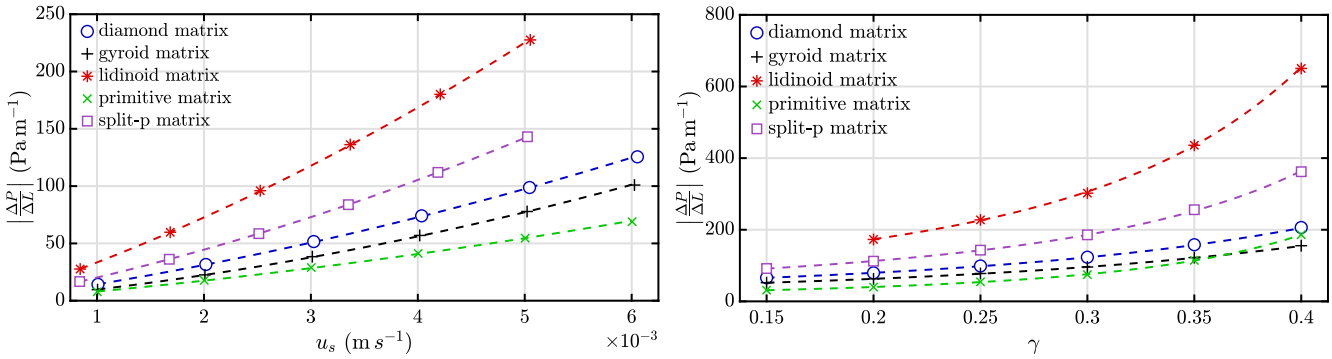

(a) Pressure drop for structures with a volume fraction of 0.25. The (−−) lines represent equation 2.

(b) Pressure drop for structures with a superficial fluid velocity of 5×10^{-3} m s^{-1}. The (−−) lines represent equation 12.

Fig. 6. Pressure drop for the examined geometries.

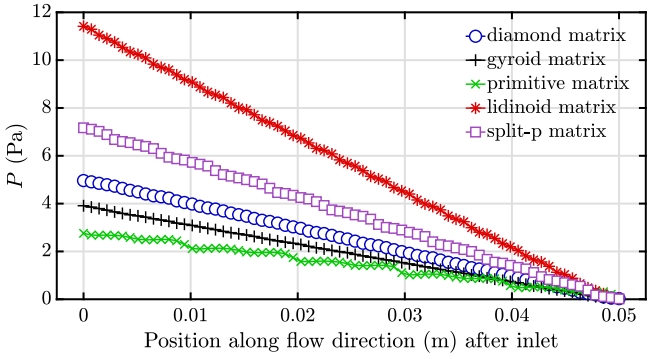

Fig. 7. Evolution of pressure within the examined structures (superficial fluid velocity = 5×10^{-3} m s^{-1}, volume fraction = 0.25).

each lattice over the range of examined volume fractions, indicating that the flow is in the Forchheimer regime. $\Delta P/\Delta L$ were therefore fit with Eq. (2) to determine the permeability constants for each lattice structure, which are plotted in Fig. 10. K_2 are four orders of magnitude larger than K_1, with both constants decreasing as volume fraction increases. Fig. 10 shows that at low volume fractions, the PM structure exhibits larger K_1 and K_2 than the GM structure. This changes at a volume fraction of $\gamma = 0.310$ for K_1 and we observe the approach of this change at $\gamma = 0.4$ for K_2. Therefore, the volume fraction at which the pressure drop intersects for the GM and PM structures in Fig. 6(b) will be in the range of 0.310–0.4, irrespective of fluid velocity.

For each examined lattice type, the following equations

$$K_1 = A_1\gamma^2 + B_1\gamma + C_1\,, \tag{10}$$

$$K_2 = A_2\gamma^2 + B_2\gamma + C_2 \tag{11}$$

were used to relate K_1 and K_2 to the volume fraction, γ, where $A_{1,2}$, $B_{1,2}$ and $C_{1,2}$ are fit parameters. Eq. (2) can then be expressed as

$$\left|\frac{\Delta P}{\Delta L}\right| = \frac{\mu\, u_s}{A_1\gamma^2 + B_1\gamma + C_1} + \frac{\rho\, {u_s}^2}{A_2\gamma^2 + B_2\gamma + C_2}\,, \tag{12}$$

which can be used to predict the pressure drop exhibited by each structure over a range of volume fractions and superficial fluid velocities. Eq. (12) describes a surface, where Fig. 11 gives the hydraulic performance of the GM lattice. Fit values for the parameters are given in Table 2, which can henceforth be used to specify the volume fraction for the examined TPMS structures to provide a pressure drop for a known flow rate.

3.2. Thermal performance

Volumetric Nusselt numbers are presented in Fig. 12. Correlations of the form

$$Nu_{vol} = F\, Re^n \tag{13}$$

were sought, where Fu et al. [16] stated that the parameters n and F are related to the geometrical features of the structure, with F also containing the Prandtl number. Fig. 12 shows that this relationship describes the data accurately. Eqs. (9) and (13) are then combined to provide

$$h_{m,vol} = \frac{F\, k\, Re^n}{{D_h}^2}\,, \tag{14}$$

which is valuable because it can be expressed in terms of u_s and γ. This is done using Eqs. (4) and (5), while D_h can also be defined as

$$D_h = 4\frac{V_w}{A_{w,s}} = 4\frac{(V_w/V_T)}{(A_{w,s}/V_T)} = \frac{4}{A_v}(1-\gamma)\,, \tag{15}$$

where V_T is the total volume of the design space. Eq. (14) can therefore be expressed as

$$\begin{aligned} h_{m,vol} &= F\, k\, {D_h}^{n-2}\left(\frac{u_s}{\nu\,(1-\gamma)}\right)^n\,, \\ &= F\, k\left(\frac{4}{A_v}\right)^{n-2}(1-\gamma)^{n-2}\left(\frac{u_s}{\nu\,(1-\gamma)}\right)^n\,, \\ &= F\, k\left(\frac{4}{A_v}\right)^{n-2}\left(\frac{u_s}{\nu}\right)^n(1-\gamma)^{-2}\,. \end{aligned} \tag{16}$$

To use Eq. (16) as a predictive model for $h_{m,vol}$ over a range of fluid velocities and volume fractions, the dependence of A_v, n and F on volume fraction must be known. It was found that A_v and n decrease with volume fraction, and are well described by $A_v = p_1\gamma^{p_2} + p_3$ and $n = n_1\gamma + n_2$. We observed no discernible relationship between F and γ, but, for each lattice type, the full range of F values was seen to fall within $\overline{F}\ \pm\ 8\%$. Therefore, F was treated as a constant by calculating its mean value. The volumetric heat transfer coefficient can then be obtained from

$$h_{m,vol} = \frac{\overline{F}\, k\left(\frac{4}{p_1\gamma^{p_2}+p_3}\right)^{n_1\gamma+n_2-2}\left(\frac{u_s}{\nu}\right)^{n_1\gamma+n_2}}{(1-\gamma)^2}\,, \tag{17}$$

with $p_{1,2,3}$, $\overline{F}$ and $n_{1,2}$ given in Table 3. This equation describes a surface and can be used to predict the volumetric heat transfer coefficient over a range of volume fractions and superficial fluid velocities. This model accurately predicts the $h_{m,vol}$ from Eq. (8), with a maximum deviation less than 10% over the examined ranges of volume fraction and flow rate.

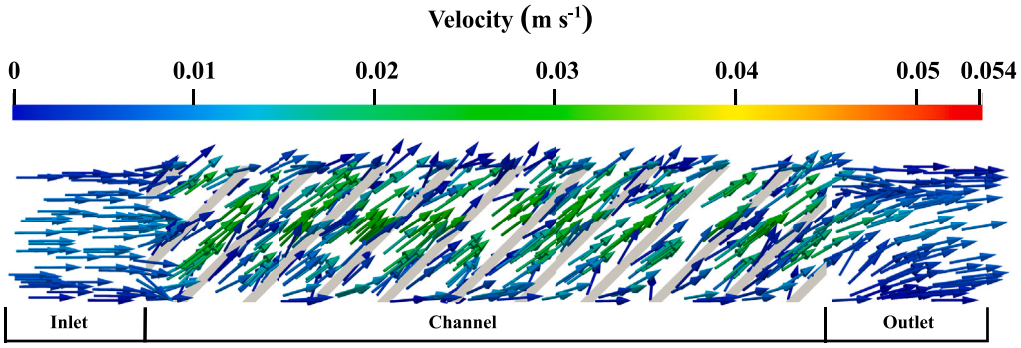

(a) Diamond matrix lattice.

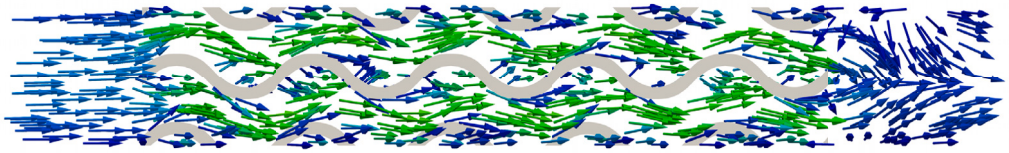

(b) Gyroid matrix lattice.

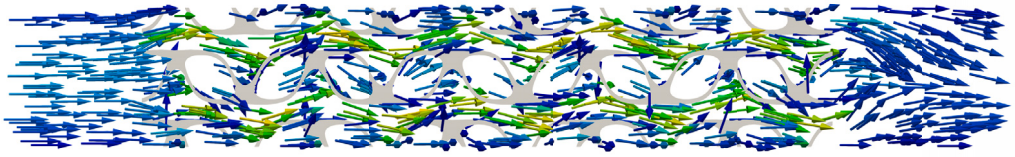

(c) Lidinoid matrix lattice.

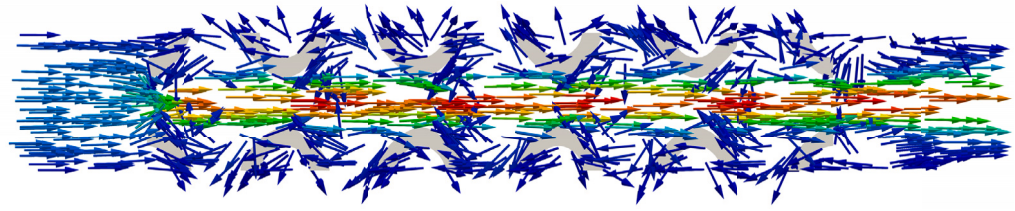

(d) Primitive matrix lattice.

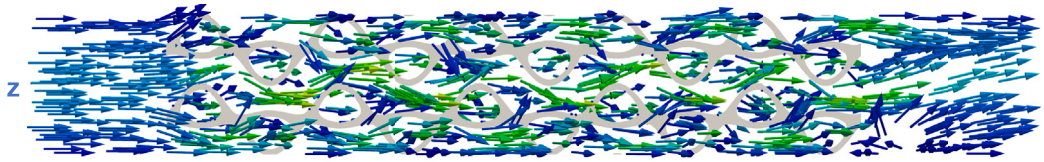

(e) Split-p matrix lattice.

Fig. 8. Fluid velocity vectors across the $x = 0.005$ m plane for structures with a volume fraction of 0.25 and a superficial fluid velocity of 5×10^{-3} m s^{-1}.

Table 2
Determined fit parameters for Eq. (12).

Lattice type	Fit parameter $\times 10^{-7}$ (m^2)			Adjusted R^2	Fit parameter $\times 10^{-3}$ (m)			Adjusted R^2
	A_1	B_1	C_1		A_2	B_2	C_2	
DM	3.4	−4.5	1.59	0.9999	5.9	−6.8	2.09	0.9999
GM	4.7	−6.3	2.35	0.9998	6.0	−6.5	1.95	0.9998
LM	2.1	−2.5	0.79	0.9995	4.9	−4.9	1.27	0.9994
PM	10.1	−12.1	3.63	0.9997	22.3	−21.6	5.44	0.9994
SPM	2.6	−3.6	1.22	0.9998	3.9	−4.7	1.42	0.9998

Table 3
Determined fit parameters for Eq. (17).

Lattice type	p_1 (m^{-1})	p_2	p_3 (m^{-1})	Adjusted R^2	$\overline{F}$	n_1	n_2	Adjusted R^2
DM	−405	2.13	768	0.9999	1.06	−0.277	0.510	0.8812
GM	−308	2.09	619	0.9998	1.21	−0.173	0.499	0.9738
LM	−847	1.92	1232	0.9990	0.52	−0.455	0.554	0.9987
PM	−305	2.23	471	0.9998	1.39	−0.135	0.431	0.9709
SPM	−580	2.13	1026	0.9999	0.63	−0.106	0.444	0.8733

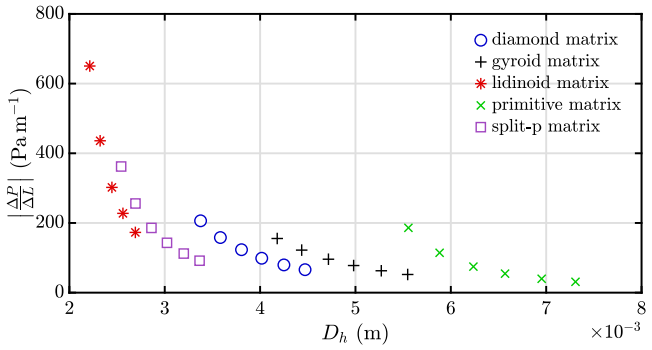

Fig. 9. Pressure drop for structures with a superficial fluid velocity of 5×10^{-3} m s^{-1}.

By comparing the predicted $h_{m,vol}$ of the examined lattice structures in Figs. 13 and 14, we found that the LM lattice exhibits the greatest volumetric heat transfer coefficient at low volume fractions, but at higher volume fractions the DM lattice has the highest volumetric heat transfer coefficient. The PM lattice exhibits the lowest volumetric heat transfer coefficient in this study.

Local effects are important in determining how the lattice geometry affects heat transfer. h_l were calculated across 70 equally spaced cross-sections along the flow direction and are shown in Fig. 15. All of the TPMS structures exhibit periodically fluctuating h_l, with the PM lattice showing the greatest variation in h_l, from 2100 to 44,000 W m^{-2} K^{-1}. Despite having the highest h_l, the PM structure also has the lowest h_l which explains why it exhibits the lowest $h_{m,vol}$. The other lattice structures have much smaller variance in h_l.

The distribution of h_l on the lattice surface further explains the differences observed in Fig. 15. For simplicity, Fig. 16 displays the distribution of h_l for the PM lattice, which was chosen due to the large variation in h_l. Peak h_l are seen in regions where the central channel diameter is narrowest. Other high h_l regions are observed outside the central channel, where the diameter is at a local minima. The fluid moves faster in these sections, as shown in Fig. 8(d), and can therefore transport more heat from the walls there. The same effect is also observed, but to a lesser extent due to the smaller variation in channel diameter, in the other examined TPMS structures. For example, h_l for the GM lattice takes values from 14,000–25,000 W m^{-2} K^{-1}, which is a much narrower range than that exhibited by the PM lattice (2100–44,000 W m^{-2} K^{-1}). From Fig. 8, we can therefore deduce that h_l is driven mainly by local fluid velocity, which itself is largely determined by channel diameter.

4. Discussion

4.1. Hydraulic performance

Santos et al. [45] calculated the permeability constants for a variety of lattice structures consisting of 4 × 4 × 4 cells in a 13 × 13 × 13 mm volume over a range of different flow regimes. Compared to the structures in the present study, those lattices have greater surface area and a larger number of cells per unit volume, and we can therefore expect the structures of Santos et al. [45] to be less permeable than the lattice structures examined here within the Forchheimer flow region. This is confirmed in Fig. 17, where the permeability constants, K_1 and K_2, for the gyroid and primitive matrix lattices in this study are up to two orders of magnitude greater than those of Santos et al. [45]. This highlights the challenge of developing general and practicable analytical relationships for the flow in these structures, as a range of geometrical properties, such as the number of cells and size of the design space, clearly have a large impact on the permeability. However, the work of Santos et al. [45] confirms our observation that the primitive matrix lattice is more permeable at lower volume fractions and the gyroid matrix is more permeable at larger volume fractions. This finding was further elaborated in the current study by examining the fluid dynamics (see Fig. 8) and evolution of pressure drop (see Fig. 7) within the structures. Sharp pressure drops were found in the primitive matrix lattice at the cell boundaries, while the gyroid matrix lattice does not exhibit this behaviour.

Dietrich et al. [15] calculated the permeability constants for foams of different materials with varying pore sizes and volume fractions. A selection of those results are compared to this study in Fig. 17. The gyroid and primitive matrix lattices possess permeabilities similar to manufactured foam. Additively manufactured surface-based lattices can therefore be a valid substitute for conventional foams in fluid flow applications, as they are hydraulically no less efficient and also possess a greater degree of tailorability due to their computer-based design method.

The Forchheimer and inertial permeabilities of lattice structures are dependent on the internal geometry, and therefore, quite clearly, the volume fraction. The fits used here (Eqs. (10) and (11)) are empirical, and do not account specifically for such factors as surface area or channel tortuosity, either of which may be found to have a predominant effect on fluid flow. A robust, general model will incorporate these, and other, geometrical factors into structure-performance relationships capable of accurately predicting fluid through any lattice type. We have made a contribution towards this goal with Eq. (12) and the parameters quoted in Table 2. These can be used to predict pressure drop over a range of volume fractions and superficial fluid velocities for the examined lattice structures. This will enable designers to make

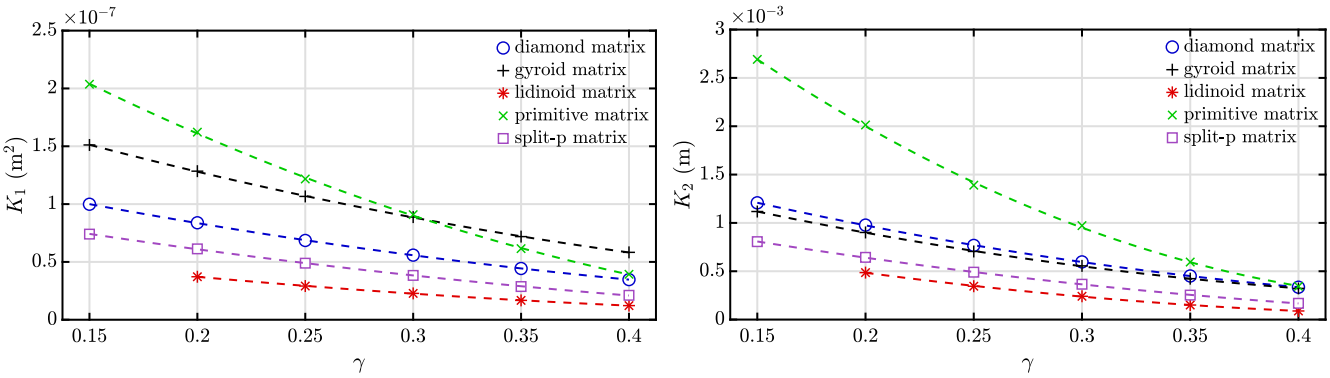

(a) Forchheimer permeability constant. The (−−) lines represent equation 10.

(b) Inertial permeability constant. The (−−) lines represent equation 11.

Fig. 10. Permeability constants as a function of volume fraction for different lattice geometries.

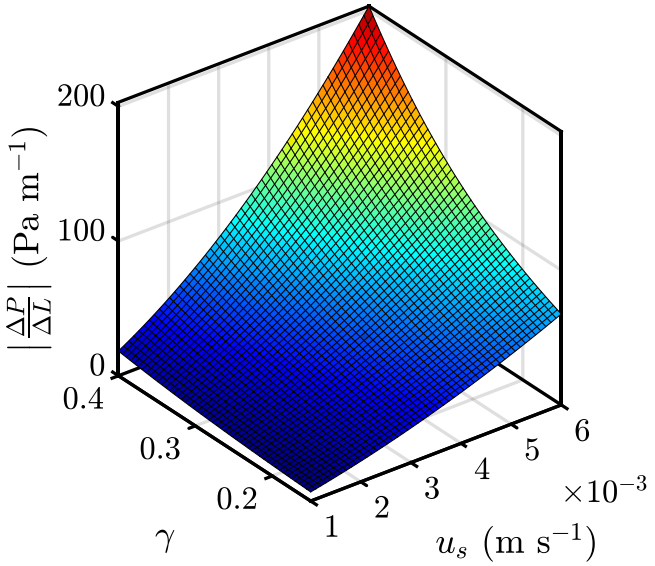

Fig. 11. Pressure drop as a function of superficial fluid velocity and volume fraction for the gyroid matrix lattice.

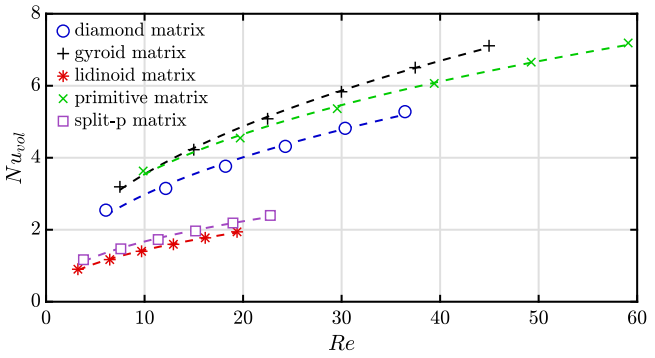

Fig. 12. Volumetric Nusselt numbers for lattice structures with a volume fraction of 0.25. The (−−) lines represent Eq. (13).

informed decisions on lattice design for fluid flow applications. These fit parameters are valid only for structures with 1 × 5 × 1 cells for a design space of 10 × 50 × 10 mm. These results are still valuable however, since flow in larger lattice structures (i.e., $N_1 \times N_2 \times N_3$ cells) is determined to a large extent by the characteristic fluid dynamics in individual cells.

4.2. Thermal performance

As discussed in Sections 3.1 and 3.2, both the pressure drop and local wall heat transfer coefficient of surface-based lattice structures are dependent on channel diameter. We would therefore expect volumetric heat transfer coefficients to correlate with pressure drop. However, this is not always the case, as the diamond matrix lattice exhibits relatively small pressure drops but high volumetric heat transfer coefficients. Hence, engineers need to inspect both the hydraulic and thermal performance in tandem to determine appropriate surface-based lattice structures for heat transfer applications.

By examining the distribution of fluid temperature in the structure which exhibited the greatest volumetric heat transfer coefficient (i.e., the diamond matrix lattice) in Fig. 18(a), we see that there is a significant amount of thermal mixing which allows the thermal energy to be transferred away from the heat input. This is in contrast to the primitive matrix lattice (which has the lowest volumetric heat transfer coefficient) in Fig. 18(b), where we see that there is minimal thermal mixing within the structure due to the high-velocity central flow channel (shown in Fig. 8(d)) which prevents the fluid from moving across it. It is also observed that there is minimal heat transfer taking place in the upper regions where the local wall heat transfer coefficient peaks (Fig. 16). This is because heat is applied to the structure only from one direction (below). Therefore, structures which (i) conduct more heat through the lattice walls far away from the heat input, and (ii) maximise thermal mixing, should boast greater volumetric heat transfer coefficients.

This theory is corroborated by the distribution of fluid outlet temperature in Fig. 19. Here, we observe that the primitive matrix lattice, which has the lowest volumetric heat transfer coefficient, has the least well distributed fluid outlet temperature and that the top half of the structure is rendered relatively ineffective for heat transfer. Following on from this, the gyroid matrix and split-p matrix lattices have the next highest volumetric heat transfer coefficients and more evenly distributed fluid outlet temperatures, though a discontinuity is still observed between the bottom and top halves of those structures. Finally, the diamond and lidinoid matrix lattices have the highest volumetric heat transfer coefficients in this study and have relatively well distributed fluid outlet temperatures indicating better fluid mixing. This is in-line with other work found, such as that of Gado et al. [40] where the improved performance of the lidinoid matrix lattice was attributed to its relatively large specific surface area.

We conclude that the thermal performance of TPMS lattice structures is heavily dependent on the internal geometry of the structure in the case of a directional heat input, where lattices that can distribute heat across the entire fluid volume exhibit greater performance. In the case of a non-directional heat input (i.e., fixed wall temperatures) the

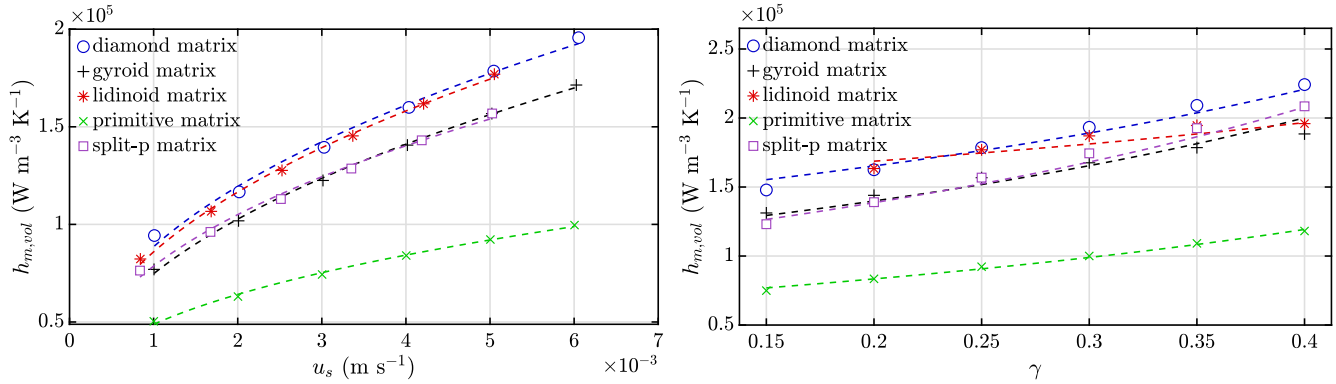

(a) Volumetric heat transfer coefficient for structures with a volume fraction of 0.25. The (−−) lines represent equation 17.

(b) Volumetric heat transfer coefficient for structures with a superficial fluid velocity of 5×10^{-3} m s^{-1}. The (−−) lines represent equation 17.

Fig. 13. Volumetric heat transfer coefficient for the examined geometries.

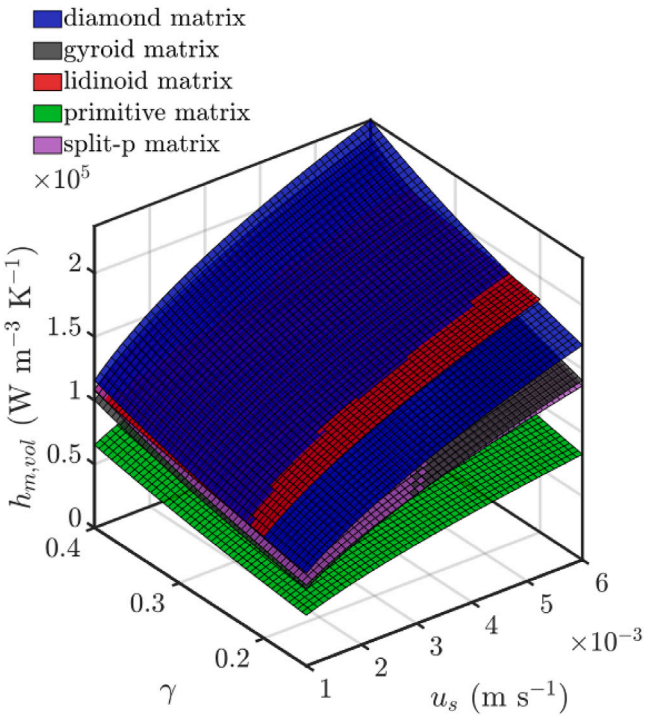

Fig. 14. Volumetric heat transfer coefficient as a function of superficial fluid velocity and volume fraction for the examined structures.

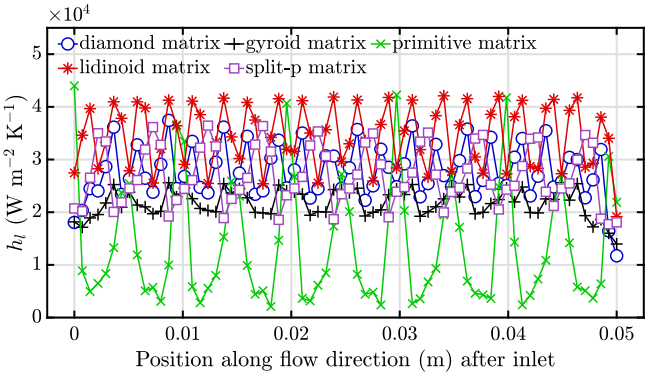

Fig. 15. Evolution of local wall heat transfer coefficient within the examined structures (superficial fluid velocity = 5×10^{-3} m s^{-1}, volume fraction = 0.25).

thermal performance will be largely determined by the channel diameter. This is in keeping with the emerging picture from investigations of TPMS lattices as heat sinks; their thermal performance is heavily dependent on lattice cell geometry [32].

Nusselt numbers for foams were previously examined by Wu et al. [17] and Fu et al. [16], who employed the relationship given in Eq. (13). The excellent agreement with this model for the lattice structures examined here (Fig. 12) confirms that these surface-based lattices can be characterised by volumetric Nusselt numbers in the same way as conventional foams. A robust, general model will be able to predict the thermal performance of surface-based lattices across a range of superficial fluid velocities and volume fractions. Eq. (17) and the parameters quoted in Table 3 contribute to this and can accurately predict the volumetric heat transfer coefficient for the examined surface-based lattice structures with $1 \times 5 \times 1$ cells in a $10 \times 50 \times 10$ mm design space. This model can be improved, and generalised to other lattice structures, by incorporating more complete descriptions of how the Nusselt parameters F and n are affected by the internal lattice geometry.

Combined with the model discussed above for hydraulic performance, surface-based lattice structures can henceforth be designed in a way which minimises their pressure drop for a given flow rate whilst achieving a specified heat transfer coefficient. This can be achieved via a simple search-based algorithm applied to their pressure drop and heat transfer relationships (i.e., the surfaces given by Eqs. (12) and (17)). The practical implication of reduced pressure drop for a given flow rate is reduced power consumption for the pumps, or fans, which move the coolant through the heat sink. Being able to design surface-based heat sinks which reduce or maintain power consumption compared to traditional designs, whilst improving heat transfer capabilities, will be important for various applications which require enhanced cooling.

5. Conclusions

This work examines the fluid flow and conjugate heat transfer of five surface-based lattices suitable for additively manufactured heat sinks. Surface roughness, which influences fluid flow, was not considered in this study. This was done to obtain more general and useful results, as surface roughness is determined by the nature of the additive manufacturing process (extrusion, laser-sintering, etc.) and cannot easily be controlled as a design parameter. Our results provide a meaningful comparison between a selection of lattice types considered for heat management. These should be validated against experimental data, particularly that from additively manufactured heat sinks.

Permeability constants for the lattice structures were calculated and used to create a predictive model for pressure drop over a range of fluid velocities and volume fractions. It was found that the lidinoid

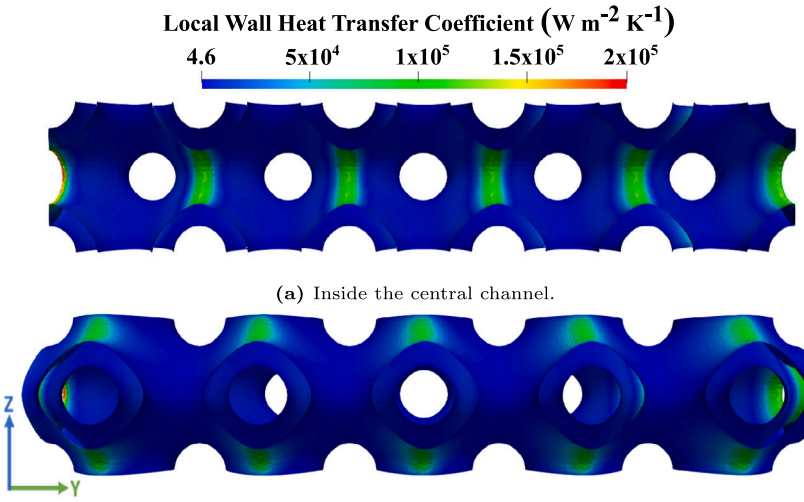

(a) Inside the central channel.

(b) Outside the central channel.

Fig. 16. Distribution of local wall heat transfer coefficient in the primitive matrix lattice (superficial fluid velocity = 5×10^{-3} m s^{-1}, volume fraction = 0.25).

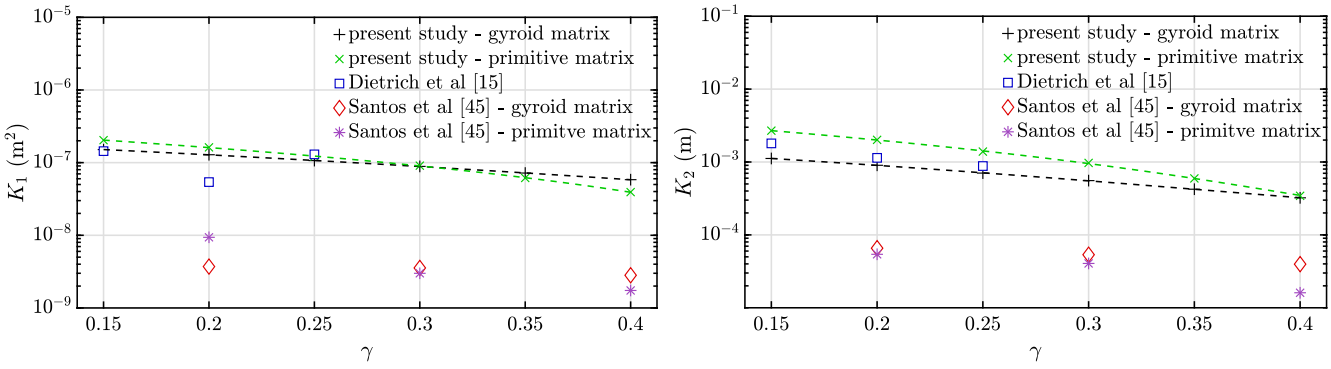

(a) Forchheimer permeability constant. The (−−) lines represent equation 10.

(b) Inertial permeability constant. The (−−) lines represent equation 11.

Fig. 17. Permeability constants of the gyroid matrix and primitive matrix structures of the current study, gyroid and primitive matrix structures [45] and a foam structure [15].

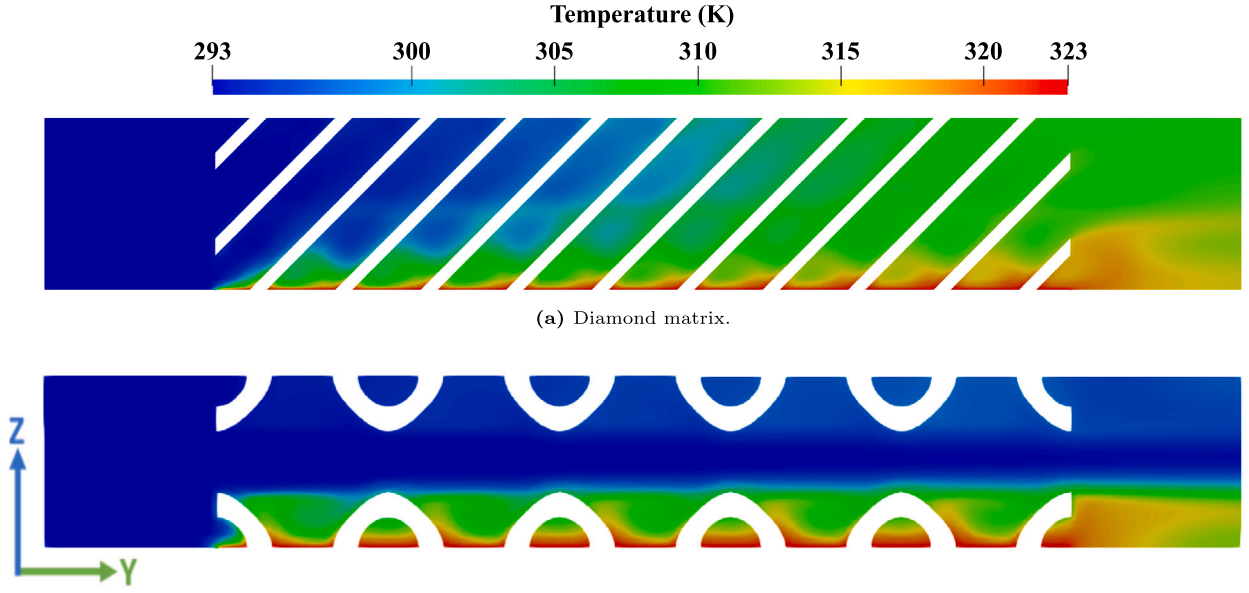

(a) Diamond matrix.

(b) Primitive matrix.

Fig. 18. Fluid temperature across the x = 0.005 m plane for the structures which exhibited the largest volumetric heat transfer coefficient (above) and the lowest volumetric heat transfer coefficient (below) (superficial fluid velocity = 5×10^{-3} m s^{-1}, volume fraction = 0.25).

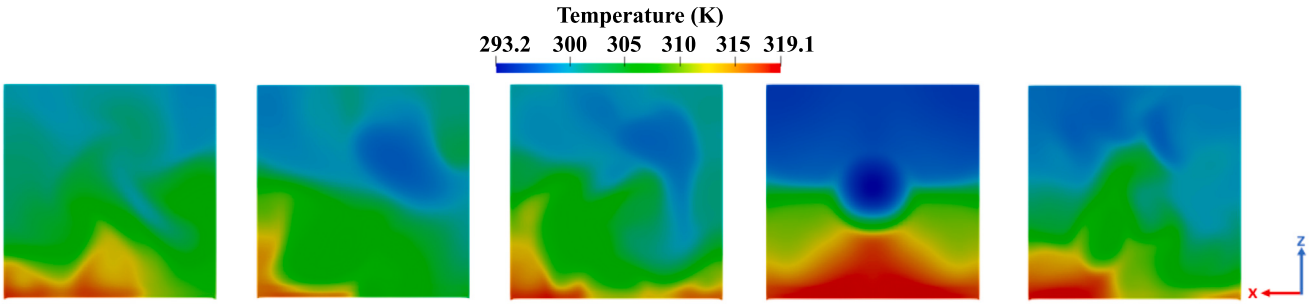

(a) Diamond matrix. (b) Gyroid matrix. (c) Lidinoid matrix. (d) Primitive matrix. (e) Split-p matrix.

Fig. 19. Distribution of outlet fluid temperature taken 1 mm from the lattice outlet (superficial fluid velocity = 5×10^{-3} m s^{-1}, volume fraction = 0.25).

matrix structure exhibited the lowest permeability constants, ranging from 1.22×10^{-8} - 3.72×10^{-8} m^2 for the Forchheimer permeability constant and 8.90×10^{-5} - 48.6×10^{-5} m for the inertial permeability constant, and therefore exhibited the greatest pressure drops from the examined structures. In contrast, the primitive matrix lattice exhibited the greatest Forchheimer permeability constants when the volume fraction was less than 0.310 and the greatest inertial permeability constants when the volume fraction was less than 0.4. The gyroid matrix lattice exhibited larger permeability constants for volume fractions above the specified values.

Relationships between volumetric Nusselt number and Reynolds number were also found and can be used to predict volumetric heat transfer coefficients for the examined structures across a range of fluid velocities and volume fractions. It was found that the primitive matrix lattice exhibited the lowest volumetric heat transfer coefficients, ranging from 4.00×10^4 - 12.7×10^4 W m^{-3} K^{-1}, and was therefore the least effective heat sink when only considering heat transfer. At relatively low volume fractions, it was found that the lidinoid matrix structure exhibited the greatest volumetric heat transfer coefficients, ranging from 7.25×10^4 - 19.6×10^4 W m^{-3} K^{-1}. At larger volume fraction however, the diamond matrix lattice exhibits the largest volumetric heat transfer coefficients, ranging from 7.07×10^4 - 24.5×10^4 W m^{-3} K^{-1}.

With these models, heat sinks based on the examined lattice structures can be designed to meet pre-defined performance requirements. It is unsuitable to extrapolate these relationships outside of the examined ranges of fluid velocity and volume fraction as they could yield erroneous results. For example, turbulent flow may have a large impact on the hydraulic and thermal performance at high Reynolds numbers.

The complex internal geometries of the lattice structures cause mixing and eddy formation, meaning they can be effective heat sinks. However, analysis of flow and fluid temperature distributions indicate that the primitive matrix lattice examined here is a poorer candidate for heat management than the other four structures, as fluid mixing is impeded by the formation of a high-velocity central flow channel. Lattice structures which are able to distribute heat across the entire fluid volume, such as the diamond matrix, are much better candidates for heat management as they maximise fluid-solid thermal interactions and fluid mixing.

New lattice structures for efficient heat sinks can be identified, or even designed from first-principles, with greater understanding of their flow and heat transfer mechanisms. Multifunctional components can also be designed using the structure-performance relationships uncovered here alongside scaling laws from other fields. Such optimised surface-based heat sinks can only be manufactured via additive manufacturing and can therefore be embedded in components of arbitrary geometry without the need for subsequent joining or assembly processes.

CRediT authorship contribution statement

D. Padrão: Conceptualization, Methodology, Software, Validation, Formal analysis, Investigation, Data curation, Writing – original draft, Writing – review & editing, Visualization. **D. Hancock:** Writing – review & editing, Supervision, Project administration, Funding acquisition. **J. Paterson:** Supervision. **F. Schoofs:** Writing – review & editing, Supervision, Project administration. **C. Tuck:** Supervision, Project administration. **I. Maskery:** Conceptualization, Software, Resources, Writing – review & editing, Supervision, Project administration, Funding acquisition.

Declaration of competing interest

The authors declare that they have no known competing financial interests or personal relationships that could have appeared to influence the work reported in this paper.

Data availability

Data will be made available on request.

Acknowledgements

This work has been part-funded by the University of Nottingham and the EPSRC Energy Programme [grant number EP/T012250/1]. We are grateful for access to the University of Nottingham's Augusta HPC service. The authors would also like to thank Mirco Magnini (University of Nottingham) for the support provided in developing the OpenFOAM model.

References

[1] I. Gibson, D. Rosen, B. Stucker, Additive manufacturing technologies: 3D printing, rapid prototyping, and direct digital manufacturing, second edition, in: D.W.D.W. Rosen, B.B. Stucker (Eds.), Additive Manufacturing Technologies: 3D Printing, Rapid Prototyping, and Direct Digital Manufacturing, Second Edition, second ed., Springer, New York, 2015, pp. 1–498.

[2] B. Blakey-Milner, P. Gradl, G. Snedden, M. Brooks, J. Pitot, E. Lopez, M. Leary, F. Berto, A. du Plessis, Metal additive manufacturing in aerospace: A review, Mater. Des. 209 (2021) 110008, URL https://linkinghub.elsevier.com/retrieve/pii/S0264127521005633.

[3] General Electric, New manufacturing milestone: 30,000 additive fuel nozzles, 2018, URL https://www.ge.com/additive/stories/new-manufacturing-milestone-30000-additive-fuel-nozzles.

[4] M.F. Ashby, Metal Foams : A Design Guide, Butterworth-Heinemann, Oxford, 2000,

[5] L.J. Gibson, in: M.F. Ashby (Ed.), Cellular Solids : Structure and Properties, second ed., in: Cambridge Solid State Science Series, Cambridge University Press, Cambridge, 1997.

[6] H.N. Wadley, D.T. Queheillalt, Thermal applications of cellular lattice structures, Mater. Sci. Forum 539–543 (2007) 242–247, URL http://www.scientific.net, https://www.scientific.net/MSF.539-543.242.

[7] T. Lu, H. Stone, M. Ashby, Heat transfer in open-cell metal foams, Acta Mater. 46 (10) (1998) 3619–3635, URL https://linkinghub.elsevier.com/retrieve/pii/S1359645498000317.

[8] J. Tian, T. Lu, H. Hodson, D. Queheillalt, H. Wadley, Cross flow heat exchange of textile cellular metal core sandwich panels, Int. J. Heat Mass Transfer 50 (13–14) (2007) 2521–2536, URL https://linkinghub.elsevier.com/retrieve/pii/S0017931007000129.

[9] O. Al-Ketan, R. Rowshan, R.K. Abu Al-Rub, Topology-mechanical property relationship of 3D printed strut, skeletal, and sheet based periodic metallic cellular materials, Addit. Manuf. 19 (2018) 167–183, http://dx.doi.org/10.1016/j.addma.2017.12.006.

[10] B. Jasperson, Y. Jeon, K. Turner, F. Pfefferkorn, W. Qu, Comparison of micro-pin-fin and microchannel heat sinks considering thermal-hydraulic performance and manufacturability, IEEE Trans. Comp. Packaging Technol. 33 (1) (2010) 148–160, URL http://ieeexplore.ieee.org/document/5286856/.

[11] D. Hancock, D. Homfray, M. Porton, I. Todd, B. Wynne, Exploring complex high heat flux geometries for fusion applications enabled by additive manufacturing, Fusion Eng. Des. 136 (2018) 454–460.

[12] J.H. Ferziger, M. Perić, R.L. Street, Computational Methods for Fluid Dynamics, fourth ed., Springer International Publishing, Cham, 2020, URL http://link.springer.com/10.1007/978-3-319-99693-6.

[13] J. Iyer, T. Moore, D. Nguyen, P. Roy, J. Stolaroff, Heat transfer and pressure drop characteristics of heat exchangers based on triply periodic minimal and periodic nodal surfaces, Appl. Therm. Eng. 209 (2022) 118192, URL https://linkinghub.elsevier.com/retrieve/pii/S135943112200148X.

[14] Z. Wu, C. Caliot, F. Bai, G. Flamant, Z. Wang, J. Zhang, C. Tian, Experimental and numerical studies of the pressure drop in ceramic foams for volumetric solar receiver applications, Appl. Energy 87 (2) (2010) 504–513, URL https://linkinghub.elsevier.com/retrieve/pii/S0306261909003122.

[15] B. Dietrich, W. Schabel, M. Kind, H. Martin, Pressure drop measurements of ceramic sponges-determining the hydraulic diameter, Chem. Eng. Sci. 64 (2009) 3633–3640.

[16] R. Viskanta, X.Fu, J. Gore, Measurement and correlation of volumetric heat transfer coefficients of cellular ceramics, Exp. Therm Fluid Sci. 17 (4) (1998) 285–293, URL https://linkinghub.elsevier.com/retrieve/pii/S089417779810002X.

[17] Z. Wu, C. Caliot, G. Flamant, Z. Wang, Numerical simulation of convective heat transfer between air flow and ceramic foams to optimise volumetric solar air receiver performances, Int. J. Heat Mass Transfer 54 (7–8) (2011) 1527–1537, URL https://linkinghub.elsevier.com/retrieve/pii/S0017931010006514.

[18] K.J. Maloney, K.D. Fink, T.A. Schaedler, J.A. Kolodziejska, A.J. Jacobsen, C.S. Roper, Multifunctional heat exchangers derived from three-dimensional micro-lattice structures, Int. J. Heat Mass Transfer 55 (9–10) (2012) 2486–2493, URL https://linkinghub.elsevier.com/retrieve/pii/S0017931012000129.

[19] J. Ho, K. Leong, T. Wong, Additively-manufactured metallic porous lattice heat exchangers for air-side heat transfer enhancement, Int. J. Heat Mass Transfer 150 (2020) 119262, URL https://linkinghub.elsevier.com/retrieve/pii/S0017931019355140.

[20] T. Dixit, P. Nithiarasu, S. Kumar, Numerical evaluation of additively manufactured lattice architectures for heat sink applications, Int. J. Therm. Sci. 159 (2021) 106607, URL https://linkinghub.elsevier.com/retrieve/pii/S1290072920310577.

[21] M. Wong, I. Owen, C. Sutcliffe, A. Puri, Convective heat transfer and pressure losses across novel heat sinks fabricated by selective laser melting, Int. J. Heat Mass Transfer 52 (1–2) (2009) 281–288, URL https://linkinghub.elsevier.com/retrieve/pii/S0017931008003311.

[22] S.M. Thompson, Z.S. Aspin, N. Shamsaei, A. Elwany, L. Bian, Additive manufacturing of heat exchangers: A case study on a multi-layered Ti–6Al–4V oscillating heat pipe, Addit. Manuf. 8 (2015) 163–174, http://dx.doi.org/10.1016/j.addma.2015.09.003.

[23] H. Brooks, K. Brigden, Design of conformal cooling layers with self-supporting lattices for additively manufactured tooling, Addit. Manuf. 11 (2016) 16–22, URL https://linkinghub.elsevier.com/retrieve/pii/S2214860416300409.

[24] E. Huttunen, M.T. Nykänen, J. Alexandersen, Material extrusion additive manufacturing and experimental testing of topology-optimised passive heat sinks using a thermally-conductive plastic filament, Addit. Manuf. 59 (2022) 103123, URL https://linkinghub.elsevier.com/retrieve/pii/S2214860422005127.

[25] C.K. Stimpson, J.C. Snyder, K.A. Thole, D. Mongillo, Roughness effects on flow and heat transfer for additively manufactured channels, J. Turbomach. 138 (5) (2016) URL https://asmedigitalcollection.asme.org/turbomachinery/article/doi/10.1115/1.4032167/378649/Roughness-Effects-on-Flow-and-Heat-Transfer-for.

[26] K.L. Kirsch, K.A. Thole, Pressure loss and heat transfer performance for additively and conventionally manufactured pin fin arrays, Int. J. Heat Mass Transfer 108 (2017) 2502–2513, URL https://linkinghub.elsevier.com/retrieve/pii/S0017931016337243.

[27] A.J. Wildgoose, K.A. Thole, P. Sanders, L. Wang, Impact of additive manufacturing on internal cooling channels with varying diameters and build directions, J. Turbomach. 143 (7) (2021) URL https://asmedigitalcollection.asme.org/turbomachinery/article/143/7/071003/1101298/Impact-of-Additive-Manufacturing-on-Internal.

[28] M. Morciano, M. Alberghini, M. Fasano, M. Almiento, F. Calignano, D. Manfredi, P. Asinari, E. Chiavazzo, 3D printed lattice metal structures for enhanced heat transfer in latent heat storage systems, J. Energy Storage 65 (2023) 107350.

[29] J. Pearl, J. Paterson, K. Flinders, N. Mantel, J.-H. You, Cyclic medium heat flux testing of a WTa lattice structure on the hive facility, Fusion Eng. Des. 194 (2023) 113699, URL https://linkinghub.elsevier.com/retrieve/pii/S092037962300282X.

[30] B. Pulvirenti, M. Celli, A. Barletta, Flow and convection in metal foams: A survey and new CFD results, Fluids 5 (3) (2020) 155, URL https://www.mdpi.com/2311-5521/5/3/155.

[31] R. Attarzadeh, M. Rovira, C. Duwig, Design analysis of the "Schwartz D" based heat exchanger: A numerical study, Int. J. Heat Mass Transfer 177 (2021) 121415, URL https://linkinghub.elsevier.com/retrieve/pii/S0017931021005184.

[32] O. Al-Ketan, M. Ali, M. Khalil, R. Rowshan, K.A. Khan, R.K. Abu Al-Rub, Forced convection computational fluid dynamics analysis of architected and three-dimensional printable heat sinks based on triply periodic minimal surfaces, J. Therm. Sci. Eng. Appl. 13 (2) (2021) URL https://asmedigitalcollection.asme.org/thermalscienceapplication/article/doi/10.1115/1.4047385/1084162/Forced-Convection-Computational-Fluid-Dynamics.

[33] Z. Cheng, R. Xu, P.-X. Jiang, Morphology, flow and heat transfer in triply periodic minimal surface based porous structures, Int. J. Heat Mass Transfer 170 (2021) 120902, http://dx.doi.org/10.1016/j.ijheatmasstransfer.2021.120902.

[34] J. Kelly, L. Finkenauer, P. Roy, J. Stolaroff, D. Nguyen, M. Ross, A. Hoff, J. Haslam, Binder jet additive manufacturing of ceramic heat exchangers for concentrating solar power applications with thermal energy storage in molten chlorides, Addit. Manuf. 56 (2022) 102937, http://dx.doi.org/10.1016/j.addma.2022.102937.

[35] I. Kaur, P. Singh, Flow and thermal transport characteristics of triply-periodic minimal surface (TPMS)-based gyroid and Schwarz-P cellular materials, Numer. Heat Transfer, Part A: Appl. 79 (8) (2021) 553–569, URL https://www.tandfonline.com/doi/abs/10.1080/10407782.2021.1872260.

[36] W. Li, W. Li, Z. Yu, Heat transfer enhancement of water-cooled triply periodic minimal surface heat exchangers, Appl. Therm. Eng. 217 (2022) 119198, URL https://linkinghub.elsevier.com/retrieve/pii/S1359431122011309.

[37] R. Attarzadeh, S.-H. Attarzadeh-Niaki, C. Duwig, Multi-objective optimization of TPMS-based heat exchangers for low-temperature waste heat recovery, Appl. Therm. Eng. 212 (2022) 118448, URL https://linkinghub.elsevier.com/retrieve/pii/S1359431122004033.

[38] G. Feng, L. Qiu, Y. Feng, X. Zhang, Topological design of open-cell microstructure with optimal effective thermal conductivity, Int. J. Heat Mass Transfer 214 (2023) 124427, URL https://linkinghub.elsevier.com/retrieve/pii/S0017931023005720.

[39] D. Mahmoud, S.R.S. Tandel, M. Yakout, M. Elbestawi, F. Mattiello, S. Paradiso, C. Ching, M. Zaher, M. Abdelnabi, Enhancement of heat exchanger performance using additive manufacturing of gyroid lattice structures, Int. J. Adv. Manuf. Technol. 126 (9–10) (2023) 4021–4036, https://link-springer-com.nottingham.idm.oclc.org/article/10.1007/s00170-023-11362-9, https://link.springer.com/10.1007/s00170-023-11362-9.

[40] M.G. Gado, S. Ookawara, H. Hassan, Utilization of triply periodic minimal surfaces for performance enhancement of adsorption cooling systems: Computational fluid dynamics analysis, Energy Convers. Manage. 277 (2023) 116657, URL https://linkinghub.elsevier.com/retrieve/pii/S0196890423000031.

[41] S.-H. Oh, J.-W. Ha, K. Park, Adaptive conformal cooling of injection molds using additively manufactured TPMS structures, Polymers 14 (1) (2022) 181, URL https://www.mdpi.com/2073-4360/14/1/181.

[42] Z.A. Qureshi, S.A.B. Al Omari, E. Elnajjar, F. Mahmoud, O. Al-Ketan, R.A. Al-Rub, Thermal characterization of 3D-printed lattices based on triply periodic minimal surfaces embedded with organic phase change material, Case Stud. Therm. Eng. 27 (2021) 101315, URL https://linkinghub.elsevier.com/retrieve/pii/S2214157X21004780.

[43] Z.A. Qureshi, E. Elnajjar, O. Al-Ketan, R.A. Al-Rub, S.B. Al-Omari, Heat transfer performance of a finned metal foam-phase change material (FMF-PCM) system incorporating triply periodic minimal surfaces (TPMS), Int. J. Heat Mass Transfer 170 (2021) 121001, URL https://linkinghub.elsevier.com/retrieve/pii/S0017931021001046.

[44] Z. Ahmed Qureshi, S. Addin Burhan Al-Omari, E. Elnajjar, O. Al-Ketan, R. Abu Al-Rub, Architected lattices embedded with phase change materials for thermal management of high-power electronics: A numerical study, Appl. Therm. Eng. 219 (2023) 119420, URL https://linkinghub.elsevier.com/retrieve/pii/S1359431122013503.

[45] J. Santos, T. Pires, B.P. Gouveia, A.P. Castro, P.R. Fernandes, On the permeability of TPMS scaffolds, J. Mech. Behav. Biomed. Mater. 110 (2020) 103932, http://dx.doi.org/10.1016/j.jmbbm.2020.103932.

[46] A. Della Torre, G. Montenegro, G. Tabor, M. Wears, CFD characterization of flow regimes inside open cell foam substrates, Int. J. Heat Fluid Flow 50 (2014) 72–82, URL https://linkinghub.elsevier.com/retrieve/pii/S0142727X14000642.

[47] I. Maskery, L. Parry, D. Padrão, R. Hague, I. Ashcroft, Flatt pack: A research-focussed lattice design program, Addit. Manuf. 49 (2022) 102510, URL https://linkinghub.elsevier.com/retrieve/pii/S2214860421006576.

[48] O. Al-Ketan, D.-W. Lee, R. Rowshan, R.K. Abu Al-Rub, Functionally graded and multi-morphology sheet TPMS lattices: Design, manufacturing, and mechanical properties, J. Mech. Behav. Biomed. Mater. 102 (2020) 103520, URL https://linkinghub.elsevier.com/retrieve/pii/S1751616119312482.

[49] OpenFOAM, URL https://www.openfoam.com/.

[50] B. Vayssette, N. Saintier, C. Brugger, M. El May, Surface roughness effect of SLM and EBM Ti-6Al-4V on multiaxial high cycle fatigue, Theor. Appl. Fract. Mech. 108 (2020) 102581, URL https://linkinghub.elsevier.com/retrieve/pii/S0167844220301579.

[51] P. Edwards, M. Ramulu, Fatigue performance evaluation of selective laser melted Ti–6Al–4V, Mater. Sci. Eng. A 598 (2014) 327–337, URL https://linkinghub.elsevier.com/retrieve/pii/S0921509314000720.

[52] K.S. Chan, M. Koike, R.L. Mason, T. Okabe, Fatigue life of titanium alloys fabricated by additive layer manufacturing techniques for dental implants, Metall. Mater. Trans. A 44 (2) (2013) 1010–1022, URL http://link.springer.com/10.1007/s11661-012-1470-4.

[53] C. Guo, S. Li, S. Shi, X. Li, X. Hu, Q. Zhu, R.M. Ward, Effect of processing parameters on surface roughness, porosity and cracking of as-built IN738LC parts fabricated by laser powder bed fusion, J. Mater Process. Technol. 285 (2020) 116788, URL https://linkinghub.elsevier.com/retrieve/pii/S0924013620302028.

[54] M.J.M.J. Rhodes, in: ProQuest (Firm) (Ed.), Introduction to Particle Technology, second ed., Wiley, Chichester, England ; Hoboken, NJ, 2008.

[55] N. Dukhan, C.A. Minjeur, A two-permeability approach for assessing flow properties in metal foam, J. Porous Mater. 18 (4) (2011) 417–424, URL http://link.springer.com/10.1007/s10934-010-9393-1.

[56] S. Ergun, Fluid flow through packed columns, Chem. Eng. Prog. 48 (1952) 89–94.

[57] F.P. Incropera, D.P. DeWitt, Fundamentals of Heat and Mass Transfer, 6th, Wiley, Hoboken, N.J., 2007.

[58] S.P. Mahulikar, H. Herwig, Fluid friction in incompressible laminar convection: Reynolds' analogy revisited for variable fluid properties, Eur. Phys. J. B 62 (1) (2008) 77–86, URL http://link.springer.com/10.1140/epjb/e2008-00115-0.